



ELSEVIER

Available online at www.sciencedirect.com



Physics Letters A 306 (2003) 227–234

PHYSICS LETTERS A

www.elsevier.com/locate/pla

Lattice Boltzmann and quantum lattice gas representations of one-dimensional magnetohydrodynamic turbulence

Linda Vahala ^a, George Vahala ^{b,*}, Jeffrey Yezpe ^c

^a Department of Electrical & Computer Engineering, Old Dominion University, Norfolk, VA 23529, USA

^b Department of Physics, William & Mary, Williamsburg, VA 23185, USA

^c Air Force Research Laboratory, 29 Randolph Road, Hanscom Field, MA 01731, USA

Received 17 September 2002; received in revised form 31 October 2002; accepted 7 November 2002

Communicated by F. Porcelli

Abstract

A simplified one-dimensional (1D) magnetohydrodynamics (MHD) is solved using a lattice Boltzmann and a quantum lattice gas model. It is shown that the magnetic field decreases the strength of the velocity shock fronts, with marked spikes in the magnetic field strength that gradually broaden in time. There is very good agreement between the lattice Boltzmann model—a representation of non-linear systems that circumvent the non-local non-linear advection by simple local non-linearities within the collision operator—and the quantum lattice gas—an algorithm that is unconditionally stable and appropriate for a hybrid quantum-classical computer.

Published by Elsevier Science B.V.

PACS: 52.30.Cv; 52.35.Ra; 52.65.Kj

Keywords: MHD turbulence; Lattice Boltzmann; Quantum lattice gas; Quantum computer

1. Introduction

Turbulence is forced to deal with spatiotemporal intermittency involving coherent structures—structures that run counter to the widely exploited simple scale-similarity local arguments like the Kolmogorov $k^{-5/3}$ energy spectrum. Some insights into fluid turbulence has been gained by examining 1D models, like Burgers equation. Since MHD turbulence involve even more complex structures, insights can be gained by

turning to the 1D magnetic field generalization [1–3] of Burgers equation which exhibit Alfvénization (the interchange of fluid and magnetic energies):

$$\begin{aligned} \frac{\partial u}{\partial t} + u \frac{\partial u}{\partial x} &= -\frac{\partial}{\partial x} \left(\frac{\mathbf{B}^2}{2} \right) + \mu \frac{\partial^2 u}{\partial x^2}, \\ \frac{\partial \mathbf{B}}{\partial t} + \frac{\partial}{\partial x} (u\mathbf{B}) &= \eta \frac{\partial^2 \mathbf{B}}{\partial x^2}. \end{aligned} \quad (1)$$

The plasma velocity $\mathbf{u} = u(x)\hat{x}$, the (divergence-free) magnetic field $\mathbf{B} = B_y(x)\hat{y} + B_z(x)\hat{z}$, μ the fluid viscosity and η is the plasma resistivity. Eq. (1) can be derived from the full MHD equations when the plasma density length scales are much longer than those of

* Corresponding author.

E-mail address: vahala@niv.physics.wm.edu (G. Vahala).

the magnetic field [1,2], resulting, to leading order, in a constant density. An important simplification in this model is the neglect of the interaction between the velocity and magnetic field through the internal energy. In the limit $\mathbf{B} \rightarrow 0$, the 1D MHD model, Eq. (1), reduces to the Burgers equation with no back pressure. With $\mathbf{B} \neq 0$, however, the MHD model exhibits a self-consistent magnetic back pressure in the fluid momentum equation.

In the inviscid limit ($\mu \rightarrow 0, \eta \rightarrow 0$), the 1D MHD model possess two (non-trivial) constants of the motion:

energy:

$$E_K + E_M = \frac{1}{2} \int dx u^2 + \frac{1}{2} \int dx (B_y^2 + B_z^2),$$

cross helicity:

$$E_H = \int dx u \sqrt{B_y^2 + B_z^2}. \quad (2)$$

The energy exchange between the velocity and magnetic field is determined by [1]

$$\begin{aligned} \frac{\partial}{\partial t} E_K &= T_{b \rightarrow u} - 2\mu Q_K, \\ \frac{\partial}{\partial t} E_M &= -T_{b \rightarrow u} - 2\eta Q_B, \end{aligned} \quad (3)$$

where the energy transfer rate ($T_{b \rightarrow u}$) from \mathbf{B} to u is

$$T_{b \rightarrow u} = \frac{1}{2} \int dx \frac{\partial u}{\partial x} (B_y^2 + B_z^2) \quad (4)$$

while the kinetic (Q_K) and magnetic (Q_B) enstrophy are

$$\begin{aligned} Q_K &= \frac{1}{2} \int dx \left(\frac{\partial u}{\partial x} \right)^2, \\ Q_B &= \frac{1}{2} \int dx \left[\left(\frac{\partial B_y}{\partial x} \right)^2 + \left(\frac{\partial B_z}{\partial x} \right)^2 \right]. \end{aligned} \quad (5)$$

Here we will develop a lattice Boltzmann representation [4–11] for the 1D MHD equations (1), and compare the results with the recently developed quantum lattice gas representation [12]. The interest in lattice Boltzmann as an alternative to the standard direct computational fluid dynamic (CFD) approach rests on its avoidance of the non-linear convective derivatives by embedding the problem into a higher dimensional (kinetic) phase space. In this way, the non-local

non-linear convective derivatives of CFD, which require the use of accurate (and computationally expensive) Riemann solvers, are replaced by local nonlinear terms within the kinetic collision operator. This leads to simple algorithms, usually explicit in form, that are ideal for parallelization on multiple PE architectures, although subject to numerical instabilities in highly nonlinear (turbulent) regimes where gradient length scales become on the order of the lattice unit and/or the development of large local flow speeds. A quantum lattice Boltzmann representation has been considered by Succi and Benzi [13] while other authors have explored various quantum lattice gas formulations [14–18]. The quantum lattice gas algorithm, on the other hand, is unconditionally stable, and is ideal for implementation (and parallelization) on a hybrid quantum-classical computer as well as on a classical computer itself.

2. Lattice Boltzmann model

The simplest lattice Boltzmann model that will recover the 1D MHD equations (1) is based on a phase space lattice with kinetic velocities $e_i = (\pm 1, \pm 2)$, $i = 1, \dots, 4$. A rest particle is not needed. At each spatial node (in this 1D case, the spatial nodes lie on the x -axis), there are 4 possible streaming directions corresponding to the velocities e_i . The BGK kinetic equations are

$$\frac{\partial f_{u,i}}{\partial t} + e_i \frac{\partial f_{u,i}}{\partial x} = -\frac{1}{\tau_u} [f_{u,i} - f_{u,i}^{\text{eq}}], \quad (6)$$

$$\frac{\partial \mathbf{f}_{B,i}}{\partial t} + e_i \frac{\partial \mathbf{f}_{B,i}}{\partial x} = -\frac{1}{\tau_B} [\mathbf{f}_{B,i} - \mathbf{f}_{B,i}^{\text{eq}}], \quad (7)$$

where $\sum_i f_{u,i} = \sum_i f_{u,i}^{\text{eq}} = u(x, t)$ and the vector distribution functions satisfy the constraints $\sum_i \mathbf{f}_{B,i} = \sum_i \mathbf{f}_{B,i}^{\text{eq}} = \mathbf{B}(x, t) = B_y \hat{y} + B_z \hat{z}$. The relaxation rates are τ_u, τ_B . The equilibrium distribution functions needed to recover the MHD equations (1) are readily shown to be, from standard Chapman–Enskog calculations [5]:

$$\begin{aligned} f_{u,i}^{\text{eq}} &= \frac{1}{10} u e_i^2 + (u^2 + \mathbf{B}^2) e_i (c_u + d_u e_i^2), \\ \mathbf{f}_{B,i}^{\text{eq}} &= \frac{1}{10} \mathbf{B} e_i + u \mathbf{B} e_i (c_B + d_B e_i^2) \end{aligned} \quad (8)$$

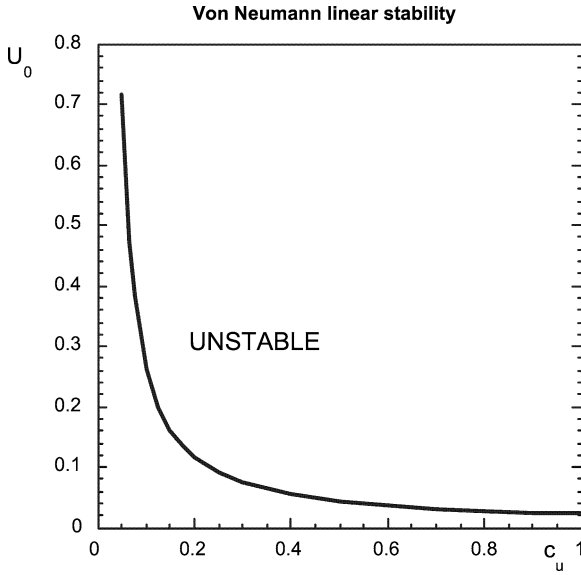


Fig. 1. The von Neumann stability plot of the maximum mean velocity U_0 versus the free parameter c_u in Eq. (8) for the lattice Boltzmann representation for Burgers equation ($\mathbf{B} \rightarrow 0$ limit) for the case $\tau_u = 0.5$.

with $34c_u + 10d_u = 0.5$, $34c_B + 10d_B = 1$ and the viscosity μ and resistivity η transport coefficients in Eq. (1) given by

$$\mu = \frac{34}{10} \left(\tau_u - \frac{1}{2} \right), \quad \eta = \frac{34}{10} \left(\tau_B - \frac{1}{2} \right), \quad (9)$$

Physically, one requires $\tau_u, \tau_B \geq 1/2$ with $\tau_u \rightarrow 0.5$ yielding infinite Reynolds number $R_e \rightarrow \infty$.

A standard von Neumann linear stability [19] on the Burgers equation (i.e., the 1D MHD equations (1) in the limit $\mathbf{B} \rightarrow 0$) puts constraints on the free parameters U_0 (equilibrium velocity) and c_u , the coefficient in the distribution function, Eq. (8). The stability curve is shown in Fig. 1 for $\tau_u = 0.5$ (which corresponds to infinite Reynolds number). For (U_0, c_u) above the stability curve, the lattice Boltzmann scheme is linearly unstable to some wave numbers, while below this curve the scheme is linearly stable to all wave numbers.

3. Quantum lattice gas model

A quantum lattice gas model for 1D MHD (with $B_y \equiv 0$) has been developed [12] by perturbatively

merging the quantum models for the diffusion and Burgers equations [17]. It should be stressed that, unlike the lattice Boltzmann method, the quantum lattice method is unconditionally stable. We briefly summarize this methodology:

Step 1. State preparation

At each spatial node x we consider a quantum computer consisting of 4 qubits so that

$$|q_a(x)\rangle = \sqrt{p_a(x)} |1\rangle + \sqrt{1 - p_a(x)} |0\rangle, \quad (10)$$

$$a = 1, \dots, 4$$

where p_a is the excited state occupation probability. From the given initial spatial profiles for the velocity and magnetic fields, one can encode at each spatial node the initial occupational levels of the excited states for each of the four qubits

$$p_1 = \frac{1}{2}(1 + u + B_z) = p_3,$$

$$p_2 = \frac{1}{2}(1 + u - B_z) = p_4 \quad (11)$$

which is reminiscent of the Elsasser variables of MHD. The on-site ket at each spatial node is just the tensor product state

$$|\psi(x)\rangle = |q_1(x)\rangle \otimes |q_2(x)\rangle \otimes |q_3(x)\rangle \otimes |q_4(x)\rangle. \quad (12)$$

Step 2. Local unitary collision interaction

At each local node, one applies a unitary collision operator \hat{U} that entangles the four on-site qubits to give the post-collision on-site ket

$$|\psi'(x)\rangle = \hat{U} |\psi(x)\rangle. \quad (13)$$

In factored quantum lattice-gas algorithms, the unitary operator does not entangle qubits on different spatial nodes.

Step 3. Measurement of post-collision occupation probabilities

Introducing \hat{n}_a , the number operator of the a th-qubit, the post-collision occupation probability

$$p'_a(x) = \langle \psi'(x) | \hat{n}_a | \psi'(x) \rangle. \quad (14)$$

The measurement process is nonunitary and destroys the quantum entanglement caused by the collision operator.

Step 4. Nearest neighbor communication

The final step of this hybrid quantum-classical (“type 2”) algorithm is to stream these post-collision probabilities to the appropriate nearest neighbors. This step, in essence, is the time-advancement of the algorithm and further advancement in time is achieved by cycling through these 4 steps. The final discretized kinetic transport equation for the post-collision probabilities is just

$$p_a(x + e_a, t + 1) = p_a(x, t) + \langle \psi(x, t) | \widehat{U}^+ \hat{n}_a \widehat{U} - \hat{n}_a | \psi(x, t) \rangle \quad (15)$$

where e_a is the streaming vector.

To specifically recover [12] the 1D MHD equations, we first consider this 4-step cycle for the square root of SWAP quantum gate¹ acting on qubits ‘3’ and ‘4’, and performing streaming only on these qubits:

$$p_a^{(1)}(x + e_a, t + 1) = p_a^{(1)}(x, t) + \langle \psi(x, t) | \widehat{U}_{\sqrt{\text{swap}}}^{(3,4)+} \hat{n}_a \widehat{U}_{\sqrt{\text{swap}}}^{(3,4)} - \hat{n}_a | \psi(x, t) \rangle, \quad (16)$$

$$e_a = (0, 0, 1, -1).$$

We now re-initialize the occupation probabilities so that

$$p_1^{(2)} = p_1^{(1)} + p_2^{(1)} + p_3^{(1)} + p_4^{(1)} = p_2^{(2)},$$

$$p_3^{(2)} = p_1^{(1)} + p_2^{(1)} - p_3^{(1)} - p_4^{(1)} = p_4^{(2)}$$

¹ The square root of SWAP gate for a 2-qubit system is the $2^2 \times 2^2$ unitary matrix $U_{\sqrt{\text{swap}}} = \begin{pmatrix} 1 & 0 & 0 & 0 \\ 0 & \frac{1-i}{2} & \frac{1+i}{2} & 0 \\ 0 & \frac{1+i}{2} & \frac{1-i}{2} & 0 \\ 0 & 0 & 0 & 1 \end{pmatrix}$. Note that

$$U_{\sqrt{\text{swap}}}^2 = U_{\text{swap}} = \begin{pmatrix} 1 & 0 & 0 & 0 \\ 0 & 0 & 1 & 0 \\ 0 & 1 & 0 & 0 \\ 0 & 0 & 0 & 1 \end{pmatrix}. \text{ The } \pi/4 \text{ rotation matrix for a 2-}$$

qubit system is defined by $U_{\pi/4} = \begin{pmatrix} 1 & 0 & 0 & 0 \\ 0 & \frac{1}{\sqrt{2}} & -\frac{1}{\sqrt{2}} & 0 \\ 0 & \frac{1}{\sqrt{2}} & \frac{1}{\sqrt{2}} & 0 \\ 0 & 0 & 0 & 1 \end{pmatrix}$. The corre-

sponding $2^4 \times 2^4$ matrices for a 4-qubit system can be immediately derived by taking appropriate tensor products with the identity matrix.

and cycle through Steps 1–4 on these re-initialized probabilities using $\pi/4$ rotation quantum gates, see footnote 1, entangling qubits ‘1’ and ‘2’ as well as entangling qubits ‘3’ and ‘4’. One then streams these post-collision probabilities with displacements $e_a = (1, -1, 1, -1)$:

$$p_a^{(2)}(x + e_a, t + 1) = p_a^{(2)}(x, t) + \langle \psi(x, t) | \widehat{U}_{\pi/4}^{(3,4)+} \widehat{U}_{\pi/4}^{(1,2)+} \hat{n}_a \widehat{U}_{\pi/4}^{(1,2)} \times \widehat{U}_{\pi/4}^{(3,4)} - \hat{n}_a | \psi(x, t) \rangle,$$

$$e_a = (1, -1, 1, -1).$$

It is very important to realize that all the above operations can be performed on an NMR quantum computer. Indeed, such a type-II quantum algorithm for the 1D diffusion equation has been realized. For the diffusion equation, one only requires 2 qubits per spatial node [17]. The experiment was performed on a liquid NMR quantum computer using a chloroform molecule. The hydrogen and a particular carbon constituted the 2 qubits. Very specific RF pulses were applied for the collisional entanglement [20]. However, one can also see this quantum algorithm as generating an unconditionally stable finite difference scheme—unconditionally stable because of the use of unitary collision operators.

To reconnect to the physics of interest, the velocity and magnetic fields are defined in terms of the stream post-collision occupation probabilities

$$u(x, t) = \frac{1}{2} [p_1^{(2)}(x, t) + p_2^{(2)}(x, t) + p_3^{(2)}(x, t) + p_4^{(2)}(x, t)], \quad (17)$$

$$B_z(x, t) = \frac{1}{2} [p_1^{(2)}(x, t) + p_2^{(2)}(x, t) - p_3^{(2)}(x, t) - p_4^{(2)}(x, t)]. \quad (18)$$

In terms of these fields, the resulting unconditionally stable finite difference scheme from this type-II quantum algorithm can be obtained. In the continuum limit, they reduce to the 1D MHD equations (11) with $B_y = 0$ to cubic errors.

However, it is formally straightforward to generalize these finite difference equations to incorporate a more general magnetic field $\mathbf{B} = B_y(x)\hat{y} + B_z(x)\hat{z}$ which in the continuum limit will reduce to the full 1D MHD equations (1). In lattice units (with x and t

integers)

$$\begin{aligned}
 u(x, t+1) &= \frac{1}{2}[u(x-1, t) + u(x+1, t)] \\
 &+ \frac{1}{4}[u^2(x-1, t) - u^2(x+1, t)] \\
 &+ \frac{1}{16}[\mathbf{B}(x-2, t) - \mathbf{B}(x+2, t)] \\
 &\times [\mathbf{B}(x-1, t) + 2\mathbf{B}(x, t) + \mathbf{B}(x+1, t)], \quad (19)
 \end{aligned}$$

$$\begin{aligned}
 \mathbf{B}(x, t+1) &= \frac{1}{4}[\mathbf{B}(x-2, t) + 2\mathbf{B}(x, t) + \mathbf{B}(x+2, t)] \\
 &+ \frac{1}{4}[u(x-1, t)\mathbf{B}(x-2, t) \\
 &+ \{u(x-1, t) - u(x+1, t)\}\mathbf{B}(x, t) \\
 &- u(x+1, t)\mathbf{B}(x+2, t)]. \quad (20)
 \end{aligned}$$

In the continuum limit, the transport coefficients are given by (with $\Delta x = 1 = \Delta t$, in lattice units)

$$\mu = \frac{(\Delta x)^2}{2\Delta t}, \quad \eta = 2\mu. \quad (21)$$

4. Simulation results

The time evolution of the initial velocity (dashed curve in Fig. 2(a)) and magnetic field (solid curves in Fig. 2(b)) profiles are presented in Figs. 2–4, using the lattice Boltzmann mode and assuming periodic boundary conditions with 512 spatial nodes. Since we will make comparison between the lattice Boltzmann and the quantum lattice gas method, see Fig. 5, it is convenient to choose parameter values $\tau_u = 0.647$ and $\tau_B = 0.794$ so as to recover the transport coefficients in Eq. (21). In Burgers turbulence ($\mathbf{B} \rightarrow 0$), regions of negative velocity gradients ($\partial u/\partial x < 0$) steepen further into shocks while the positive gradients are weakened. With $\mathbf{B} \neq 0$, the rate of time decay of the *positive* slope in the velocity field is unchanged from the Burgers equation. However, the rate of steepening of the *negative* slope region in the velocity field is somewhat arrested by the presence of the magnetic field as well as the introduction of inflection points. (Fig. 2(a)). In these $\partial u/\partial x < 0$ regions, there is strong amplification of the magnetic field, Fig. 2(b): initially we choose a small constant $B_y = +0.05$,

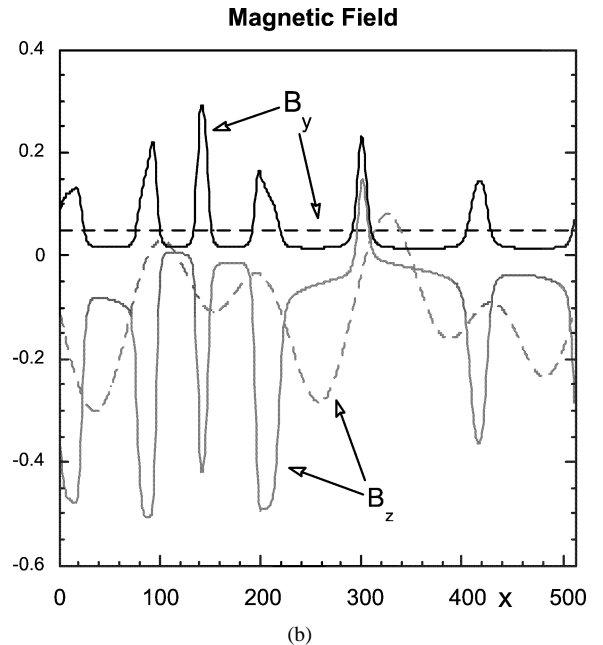
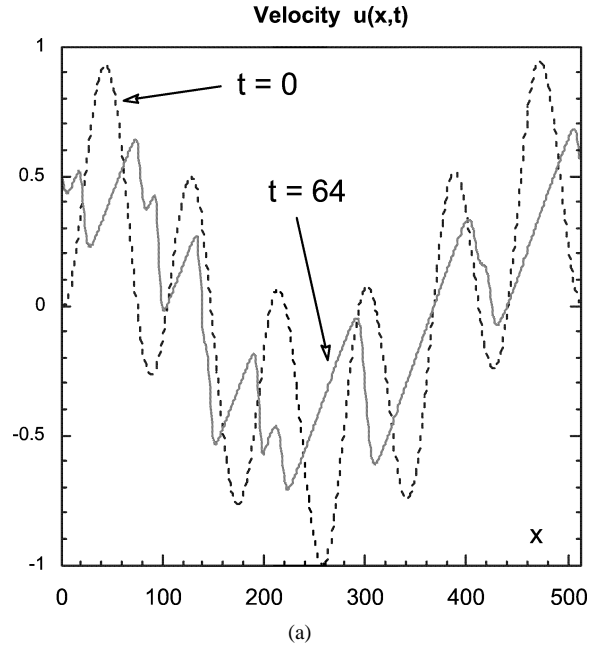


Fig. 2. (a) The evolution of the velocity profile from $t = 0$ (dashed) to $t = 64$ (solid). Regions of $\partial u/\partial x < 0$ steepen into shocks—but these shocks are weakened by the magnetic field. The time evolution of the decay of $\partial u/\partial x > 0$ are unaffected by the magnetic field. The shocks also exhibit inflection points, this not seen in simple Burgers evolution. (b) The magnetic field at $t = 0$ (dashed curves: note that $B_y = 0.05$) and $t = 64$ (solid). Note the strong enhancement in both components of \mathbf{B} —with these spikes localized to the shock regions in the velocity field.

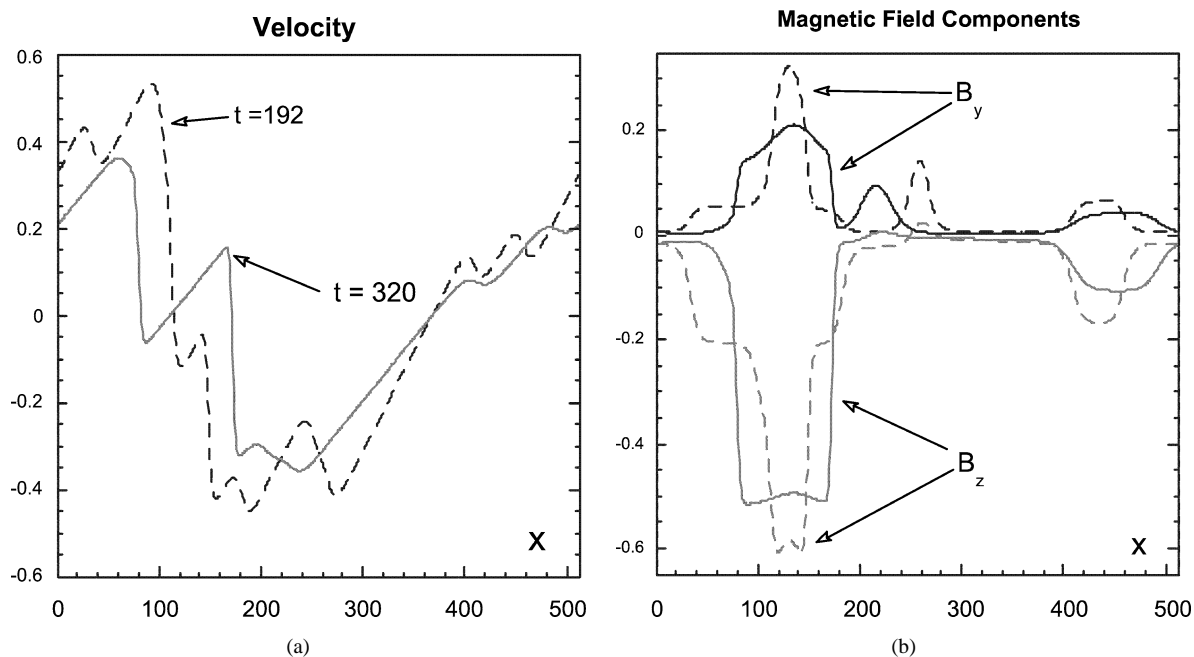


Fig. 3. (a) Velocity profiles at $t = 192$ (dashed) and $t = 320$ (solid). The shock fronts dictate the spatial positions where the magnetic field is enhanced. (b) The corresponding magnetic field at $t = 192$ (dashed) and $t = 320$ (solid). The magnetic spikes, whose sides coincide with the velocity shocks, broaden in time while the maxima decay slowly.

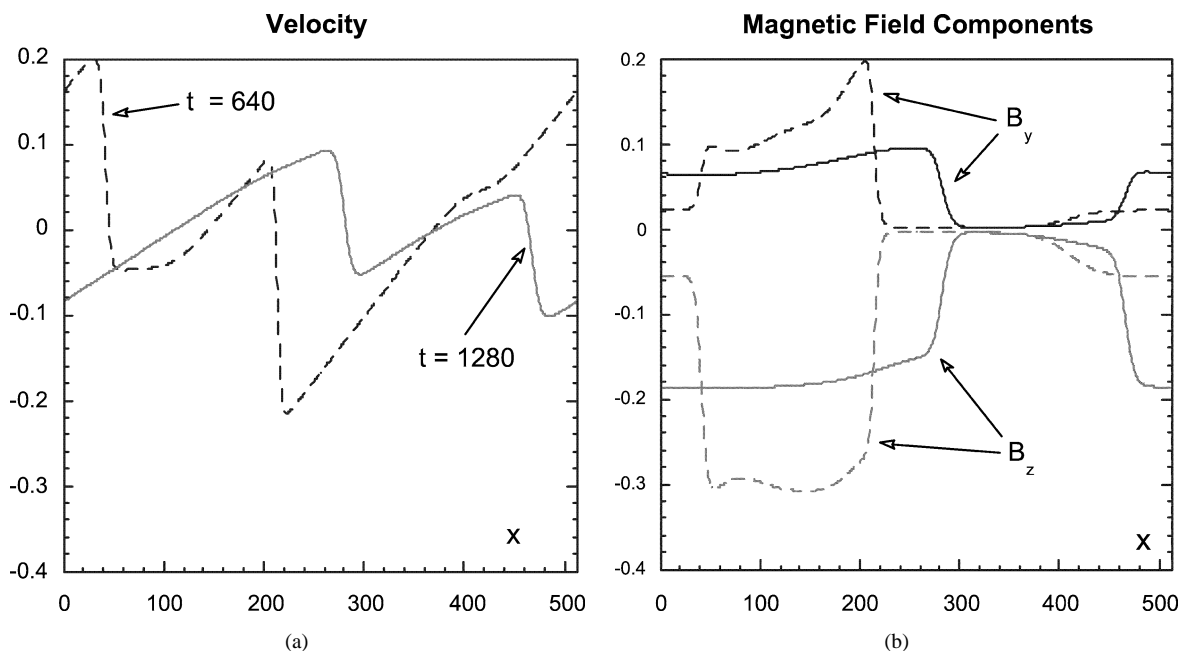


Fig. 4. (a) The velocity profiles at $t = 640$ (dashed) and $t = 1280$ (solid). At $t = 1280$, the shocks are located around $x = 280$ and $x = 470$. (b) The corresponding magnetic field components at $t = 640$ (dashed) and $t = 1280$ (solid). The magnetic shocks at $t = 1280$ occur around $x = 280$ and $x = 470$.

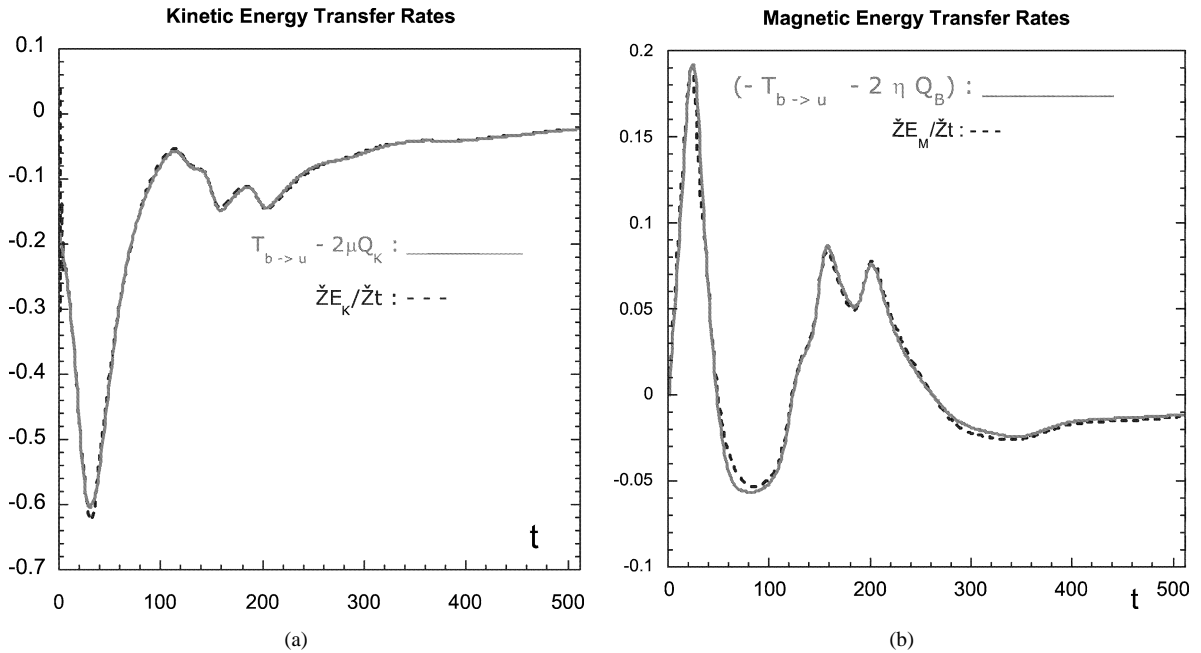


Fig. 5. (a) Lattice Boltzmann evolution of the kinetic energy on a grid of 512 lattice points. The dashed curve is $\partial E_K / \partial t$ while the solid curve is $T_{b \rightarrow u} - 2\mu Q_K$, defined in Eqs. (2)–(5). (b) Lattice Boltzmann evolution of the magnetic energy on a grid of 512 lattice points. The dashed curve is $\partial E_M / \partial t$ while the solid curve is $-T_{b \rightarrow u} - 2\eta Q_B$, defined in Eqs. (2)–(5).

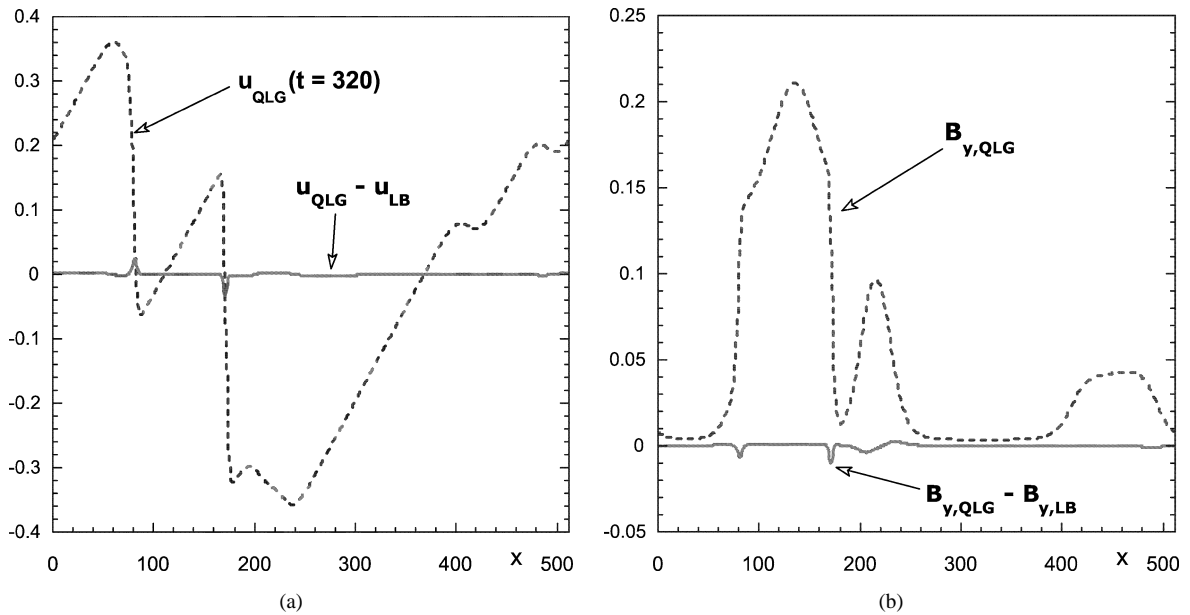


Fig. 6. (a) The difference Δu in the velocity profile at $t = 320$ between the quantum lattice gas and lattice Boltzmann algorithms. Discrepancies lie at the very sharp shocks around $x = 80$ and 170 with the algorithms differing only slightly in the spatial positions of the shocks. The solid curve is u as determined by the quantum algorithm while the dashed curve exhibits the difference in the velocity between the two algorithms. (b) The corresponding difference in the magnetic field component B_y at $t = 320$ between the quantum lattice gas and lattice Boltzmann algorithms. The solid curve is B_y as determined by the quantum algorithm, while the dashed curve exhibits the difference in B_y between the two algorithms.

while B_z is larger and non-constant (dashed curves in Fig. 2(b)). At $t = 64$, the \mathbf{B} -field becomes basically constant except for spikes located at the velocity shocks. Interesting, at $x = 300$, there is a positive spike in B_z .

The time evolution of the velocity and magnetic field profiles are shown in Figs. 3 and 4. The width of the magnetic field spikes broaden with time, with its sides located at the position of the velocity shocks. By $t = 1280$, there are only two shocks left in the velocity field with its maximum reduced by an order of magnitude.

The kinetic energy and magnetic energy decay rates, Eq. (3), are computed by the lattice Boltzmann method. In Fig. 5(a) we plot the time decay of the kinetic energy $\partial E_K/\partial t$ (dashed curve) and compare it to the energy transfer rate from the velocity field $T_{b \rightarrow u} - 2\mu Q_K$, the right-hand side of Eq. (3). The corresponding comparison of the time decay of the magnetic energy $\partial E_M/\partial t$ (dashed curve) to the energy transfer rate from the magnetic field, $-T_{b \rightarrow u} - 2\eta Q_M$ is shown in Fig. 5(b). There is excellent agreement.

Finally, in Fig. 6, we plot the velocity and magnetic field at $t = 320$ using the quantum lattice gas algorithm and compare these results determined from the lattice Boltzmann algorithm (shown in Fig. 3). There is excellent agreement between the two algorithms, with discrepancies arising around $x = 80$ and $x = 170$ in the vicinity of the velocity shocks. These discrepancies are extremely narrow and indicate that there is a very small shift in the spatial location of the shocks.

Acknowledgements

This work was supported by AFOSR.

References

- [1] S. Yanase, Phys. Plasmas 4 (1997) 1010.
- [2] J. Fleischer, P.H. Diamond, Phys. Rev. E 58 (1998) R2709; J. Fleischer, P.H. Diamond, Phys. Rev. E 61 (2000) 3912.
- [3] S. Glatier, Astrophys. J. 521 (1999) 483.
- [4] G. McNamara, G. Zanetti, Phys. Rev. Lett. 61 (1988) 2332.
- [5] F. Higuera, J. Jimenez, Europhys. Lett. 9 (1989) 633.
- [6] F. Higuera, S. Succi, R. Benzi, Europhys. Lett. 9 (1989) 345.
- [7] R. Benzi, S. Succi, M. Vergassola, Phys. Rep. 222 (1992) 145.
- [8] S. Chen, G. Doolen, Annu. Rev. Fluid Mech. 30 (1998) 329.
- [9] D. Wolf-Gladrow, Lattice-Gas Cellular Automata and Lattice Boltzmann Models, in: Lecture Notes in Mathematics, Vol. 1725, Springer-Verlag, Heidelberg, 2000.
- [10] S. Chen, H. Chen, D. Martinez, W. Matthaeus, Phys. Rev. Lett. 67 (1991) 3777; H. Chen, W. Matthaeus, Phys. Rev. Lett. 58 (1987) 1845.
- [11] S. Succi, R. Benzi, M. Vergassola, Phys. Rev. A 43 (1991) 4521.
- [12] J. Yepez, G. Vahala, L. Vahala, Phys. Rev. E, submitted for publication.
- [13] S. Succi, R. Benzi, Physica D 69 (1993) 327; S. Succi, Phys. Rev. E 55 (1997) 5261; S. Succi, Inter. J. Mod. Phys. C 8 (1997) 717; S. Succi, J. Phys. A 31 (1998) 2321.
- [14] I. Bialynicki-Birula, Phys. Rev. D 49 (1994) 6920.
- [15] D.A. Meyer, J. Stat. Phys. 85 (1996) 551; D.A. Meyer, Phys. Lett. A 223 (1996) 337; D.A. Meyer, Phys. Rev. E 55 (1997) 5261; D.A. Meyer, Int. J. Mod. Phys. C 8 (1997) 717; D.A. Meyer, J. Phys. A 31 (1998) 2321.
- [16] B.M. Boghosian, W. Taylor, Phys. Rev. E 8 (1997) 705; B.M. Boghosian, W. Taylor, Physica D 120 (1998) 30.
- [17] J. Yepez, Int. J. Mod. Phys. C 9 (1998) 1587; J. Yepez, Int. J. Mod. Phys. C 12 (2001) 1273; J. Yepez, Phys. Rev. E 63 (2001) 046702; J. Yepez, J. Stat. Phys. 107 (2002) 203.
- [18] J. Yepez, B.M. Boghosian, Comput. Phys. Commun. 146 (2002) 280.
- [19] J.D. Sterling, S. Chen, J. Comput. Phys. 123 (1996) 196.
- [20] M.A. Pravia, Z. Chen, J. Yepez, D.G. Cory, Comput. Phys. Commun. 146 (2002) 339.